Research Square

Preprints are preliminary reports that have not undergone peer review.
They should not be considered conclusive, used to inform clinical practice,
or referenced by the media as validated information.

Continuous harvesting of intermittent and continuous heats by a mixed ion/electron thermoelectric generator using an ionogel blended with carbon nanotube ionogels

Yao Wang
National University of Singapore
Qi Qian
National University of Singapore
Jianyong Ouyang
mseoj@nus.edu.sg

National University of Singapore

Article

Keywords: ionogel, ionic thermoelectrics, carbon nanotubes, MTEG, Soret effect

Posted Date: August 3rd, 2026

DOI: https://doi.org/10.21203/rs.3.rs-10420808/v1

License: This work is licensed under a Creative Commons Attribution 4.0 International License.
Read Full License

Additional Declarations: No competing interests reported.

Continuous harvesting of intermittent and continuous heats by a mixed ion/electron thermoelectric generator using an ionogel blended with carbon nanotube ionogels

Keywords: ionogel; ionic thermoelectrics; carbon nanotubes; MTEG; Soret effect

Abstract

Ionic thermoelectric (TE) materials have drawn considerable interest because their thermopower can far exceed that of conventional electronic TE materials. They are typically implemented in ionic thermoelectric capacitors (ITECs) for heat harvesting. However, ITECs can harvest only intermittent heat, and there is no electricity generation under steady temperature. Here, we demonstrate a mixed ion/electron thermoelectric generator (MTEG) that can continuously harvest both intermittent and continuous heats into electricity. The active layer is an ionogel blended with single-walled carbon nanotubes (SWNTs), forming a mixed conductor in which the ionic liquid enables ion transport while the SWNT network provides electronically conductive pathways. Under a constant temperature gradient, the MTEG delivers a stable output voltage to an external load, closely resembling the behavior of conventional thermoelectric generators. The thermopower exceeds 11.3 $mV \cdot K^{-1}$, which is 1–2 orders of magnitude higher than the Seebeck coefficient of the best electronic TE materials. This operation is attributed to synergistic effects: hole tunneling across the SWNT network coupled with the large ionic thermopower arising from the Soret effect.

1. Introduction

Heat is widely used in domestic and industrial activities, yet the overall utilization efficiency is often below 30%, with the majority dissipated as waste heat [1-5] . Waste heat is continuously generated not only during equipment operation but also through natural processes such as photothermal and geothermal pathways. Improving the conversion of this distributed thermal energy into electricity is therefore of considerable scientific and technological importance [6-12]. In this context, thermoelectric (TE) conversion is particularly attractive for low-grade heat, which is estimated to account for roughly two thirds of the total waste heat on Earth.The conventional TE materials are electronic materials, such as and inorganic semiconductor, conducting polymers, and their composites. These materials operate via the Seebeck effect, where a temperature gradient drives the redistribution of electrons or holes and produces a voltage across the sample. Their performance is commonly assessed using the dimensionless figure of merit (ZT), $ZT = \sigma S^2 T/\lambda$, where σ, S and λ represent electrical conductivity, Seebeck coefficient, and thermal conductivity, respectively. Despite substantial advances, the properties of electronic TE materials remain inadequate for many large-area and low-grade waste-heat applications. A central limitation is their relatively small thermopower, with Seebeck coefficients typically well below 1 $mV \cdot K^{-1}$ [13-17].

Ionic TE materials, including electrolytes, hydrogels, and ionogels, have emerged as promising alternatives because they can exhibit thermopowers of tens of $mV \cdot K^{-1}$, exceeding electronic counterparts by 2 to 3 orders of magnitude [18-24]. Under a temperature gradient, cations and anions undergo thermodiffusion and accumulate at opposite ends of the material, a phenomenon widely described as the Soret effect [25-31]. Under a temperature gradient, cations and anions undergo thermodiffusion and accumulate at opposite ends of the material, a phenomenon widely described as the Soret effect [32-34]. As a result, they are generally implemented in ionic thermoelectric capacitors (ITECs), where heat is harvested through thermally driven ionic polarization. A critical consequence is that ITECs generate electricity primarily during temperature fluctuations and do not provide sustained power under a steady temperature gradient. Considerable efforts have been devoted to enabling ionic TE systems to harvest heat under steady temperature gradients [35, 36]. Two device strategies have been reported. One strategy integrates an ITEC with a traditional electronic TEG [37]. This configuration allows intermittent harvesting through the ITEC and continuous operation through the electronic TEG, but the ionic component does not contribute to steady-state conversion, so the output remains limited by the low Seebeck voltage of the electronic material. A second strategy introduces ionic thermoelectric generators (ITEGs) by incorporating Soret-driven ionic polarization into thermogalvanic cells (TGCs) [38, 39] . Nevertheless, continuous power delivery remains challenging, since operation typically proceeds through multiple stages, effective heat harvesting occurs only in a specific stage, the output voltage decays markedly during this stage, and regeneration is often required after several

hours of operation. These constraints highlight the need for device concepts that preserve the large ionic thermopower while enabling steady-state electrical delivery.A significant advance toward this goal is the mixed ion/electron thermoelectric generator (MTEG). Qian et al. [40] reported MTEGs based on ionogels blended with reduced graphene oxide (rGO), which continuously harvest heat under both fluctuating and steady temperature gradients . Under steady gradients, the device response resembled that of conventional electronic TEGs, while the thermopower reached 7.0 $mV \cdot K^{-1}$. Their interpretation emphasized the coupling between ionic thermopower arising from the Soret effect and hole tunneling through the rGO network. Since electronic filler loading and conductivity critically determine electronic percolation and mixed transport, further studies using alternative conductive fillers are necessary to clarify how electronic pathways regulate TE conversion in MTEGs.

Here, we demonstrate MTEGs based on ionogels blended with single-walled carbon nanotubes (SWNTs). The resulting SWNT ionogels function as mixed ion/electron conductors, where the ionic liquid (IL) provides ionic transport and the SWNT network establishes electronically conductive pathways. In contrast to two-dimensional rGO, SWNTs are one-dimensional conductors and typically exhibit higher intrinsic electronic conductivity, which can reduce the percolation threshold within ionogels. The SWNT-based MTEGs continuously generate electricity under both fluctuating and steady temperature gradients. Under $\Delta T = 3$ K, with a 40 kΩ external load, the output voltage reaches about 29 mV, and remains clearly measurable after 16 h of continuous operation.Consistent with the lower percolation threshold of SWNTs in ionogels, the optimal SWNT loading for maximizing MTEG thermoelectric performance is substantially lower than that reported for rGO-based systems.

2. Result and discussion

2.1 Structure and properties of SWNT iongels

Figure 1a shows the chemical structures of SWNTs, sodium dodecyl sulfate (SDS), gelatin and 1-ethyl-3-methylimidazolium dicyanamide (EMIM:DCA) as ionic liquid. Gelatin serves as the gelator to immobilize EMIM:DCA, and SDS is adopted to stabilize SWNTs in water. Aqueous dispersions of SWNTs were prepared by ultrasonication of SWNTs and SDS in water. The conductivity of the SWNT/SDS films prepared from the aqueous dispersion is 3.90×10^3 S m^{-1}, and its Seebeck coefficient is 64.9 $\mu V \cdot K^{-1}$ (**Figure S1**). The σ and S are greatly higher than that (200 S m^{-1} and 17.5 $\mu V \cdot K^{-1}$) of the rGO/SDS films by Qian et al [40] .

The SWNT ionogel was fabricated following the schematic procedure in **Figure S2**. Briefly, an aqueous SWNT dispersion containing SDS was introduced into an aqueous gelatin solution that also contained SDS. The resulting mixture was drop cast onto a glass substrate and allowed to dry at room temperature for 24 h. They are transparent at the absence of SWNT, and they are black at the presence of SWNTs (**Figures 1b** and **1c**). The SWNT loading

is expressed as the weight fraction of SWNTs relative to the total mass of the ionogel constituents, namely SWNTs, gelatin, EMIM:DCA, and SDS.

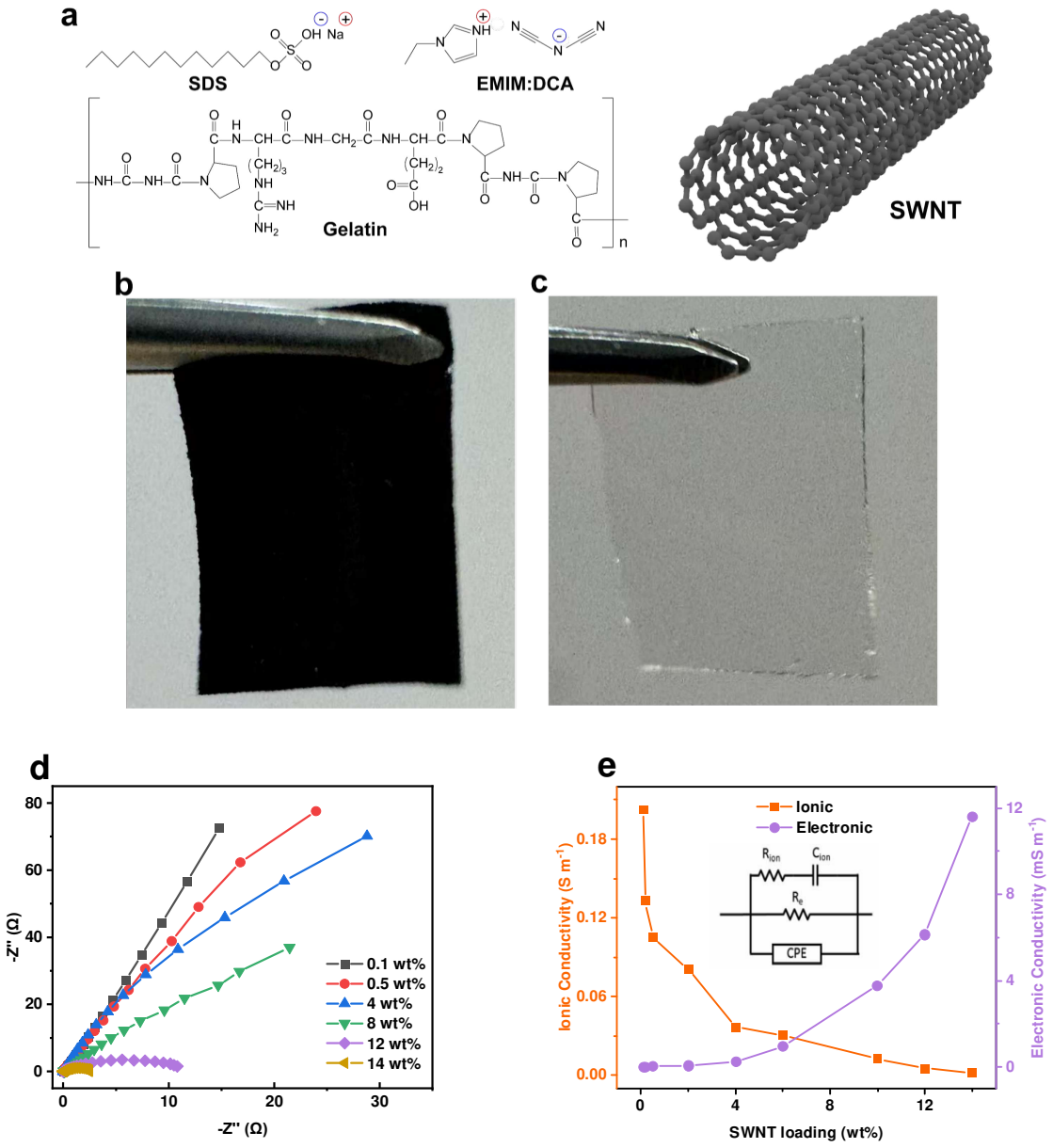


Figure 1. (a) Chemical structures of SDS, EMIM:DCA, gelatin, and SWNTs. Photographs of ionogel films containing (b) 5 wt% SWNTs and (c) 0 wt% SWNTs. (d) Nyquist plots of SWNT ionogels at different SWNT loadings, with loadings indicated. (e) Ionic and electronic conductivities as a function of SWNT loading. The inset shows the equivalent circuit used to fit the Nyquist plots.

As shown in **Figure S3**, SWNTs establish interconnected networks within the ionogels. Raman spectroscopy was used to characterize the ionogels (**Figure S4a**). For the SWNT ionogel, a peak at 1347 cm^{-1} is assigned to the D band of SWNTs, which is associated with disorder and defect sites in the carbon framework. A second peak at

1589 cm^{-1} corresponds to the G band, arising from in-plane vibrational modes of sp2-hybridized carbon atoms [41]. The dominance of the *G* band intensity over the *D* band indicates a low defect density. In the range of 2100–2300 cm^{-1}, both the ionogel with and without SWNTs show a single Raman band, which appears at 2204 cm^{-1} for the ionogel without SWNTs and shifts to 2192 cm^{-1} upon incorporation of SWNTs. This Raman feature is assigned to the C≡N stretching vibration of DCA^-, and the observed red shift suggests an interaction between SWNTs and EMIM:DCA. The ionogels were further examined by attenuated total reflection Fourier-transform infrared (ATR-FTIR) spectroscopy (**Figure S4b**). For the control ionogel without SWNTs, three bands at 2133, 2200, and 2239 cm^{-1} are evident and are attributed to the C≡N stretching vibrations of DCA^- (**Figure S4c**) [42] . At the SWNT loading of 1 wt%, these bands shift to 2122**,** 2189, and 2224 cm^{-1}**,** respectively. The red shifts also indicate the interactions between SWNTs and EMIM:DCA [43, 44] .

Dynamic mechanical analysis (DMA) was performed to evaluate the ionogels. **Figure S5a** shows the frequency (*f*) dependence of the storage modulus (*G′*) and loss modulus (*G″*) for the ionogel containing 0.5 wt% SWNTs, together with the ionogel without SWNTs. *G′* and *G″* denote the elastic and viscous components of the samples, respectively. *G′* is substantially higher than *G″* for both ionogels, which confirms their gel behavior. In addition, both *G'* and *G"* of the SWNT ionogels are greater than the ionogel without SWNT. This indicates that SWNTs can reinforce the ionogel. This can be attributed to the high mechanical strength of SWNTs and the interaction between SWNTs and EMIM:DCA. The dynamic viscosities (η'') was calculated from *G"* using $\eta'' = G''/2\pi f$ (**Figure S5b**). Across the entire frequency range, the SWNT ionogel shows substantially higher η'' than the control ionogel without SWNTs.

Because SWNTs and EMIM:DCA are electronic and ionic conductors, respectively, the SWNT ionogels can be mixed ion/electron conductors. The electronic and ionic conductivities of the SWNT ionogels were evaluated using AC impedance spectroscopy (**Figures 1d** and **S6**). In the absence of SWNTs, the Nyquist response is essentially linear. The ionic conductivity of the control ionogel is 0.44 $S \cdot m^{-1}$, determined from the intercept of the curve with the *Z*' axis. Similarly, at SWNT loadings of 0.3 wt% or below, the Nyquist plots remain nearly linear, consistent with the behavior reported for neat ionic conductors [40]. When the SWNT loading is raised to 0.5 wt% or above, the Nyquist traces exhibit a pronounced downward curvature. At loadings of 10 wt% and higher, a distinct semicircular feature emerges. This evolution is attributed to the development of electronically conductive pathways formed by SWNT networks within the ionogels.

The ionic and electronic conductivities at various SWNT loadings were determined by fitting the Nyquist plots with the equivalent circuit shown in the inset of **Figure 1e**. Within this circuit, R_{ion} and R_e correspond to the ionic and electronic resistances, respectively, and the constant phase element (CPE) represents a non-ideal capacitive

response. The CPE reflects the combined contributions from the bulk components as well as interfacial effects, including the interfaces between SWNTs and EMIM:DCA and between the ionogel and electrodes. The R_{ion} and R_e are plotted against SWNT loading in **Figures 1e** and **S7**. With increasing SWNT loading from 0.1 wt% to 14 wt%, the electronic conductivity of the ionogels rises from 0.0056 to 11.6 $mS \cdot m^{-1}$, whereas the ionic conductivity drops from 0.203 to 2.12×10^{-3} $S \cdot m^{-1}$. This reduction in ionic conductivity is ascribed to the lower ionic liquid fraction at higher SWNT contents, along with SWNT-driven stiffening of the ionogel matrix as supported by the dynamic mechanical measurements. The electronic conduction arises from the SWNTs within the ionogels. Compared with the rGO ionogels reported by Qian et al. at 16.2 wt% rGO, which exhibit an electronic conductivity of 1.7×10^{-3} $S \cdot m^{-1}$ and an ionic conductivity of 0.041 $S \cdot m^{-1}$, the present ionogel at 14 wt% SWNT shows higher electronic conductivity but lower ionic conductivity [40]. These differences arise from the higher conductivity and one-dimensional network of SWNTs.

The Nyquist plots were fitted using an equivalent circuit in which R_{ion} and R_e are in parallel. (**Figure S8**). The ionic and electronic conductivities are quite close to those obtained using the equivalent circuit in **Figure 1e**.

The electronic conductivity (σ_e) as a function of SWNT loading was analyzed using a percolation model. $\sigma_e = \sigma_0 (\phi - \phi_c)^d$, where ϕ is the volume fraction of SWNT, ϕ_c is the percolation threshold, d is the transport exponent, and σ_0 is the fitting parameter (**Figure S9**) [41]. This observation is in line with the marked change in the Nyquist response from linear to arch-like upon increasing the SWNT loading from 0.10 wt% to 14 wt% (**Figure 1d**). The fitted ϕ_c is 0.0032, corresponding to an SWNT loading of 0.52 wt% based on an SWNT density of 1.9 $g \cdot cm^{-3}$[45]. This ϕ_c value (0.0032) is notably lower than that (0.027) of the rGO [40]. This difference is consistent with the relationship between the percolation threshold and the dimensionality of the nanofillers [46, 47].

2.2 Thermoelectric properties of SWNT ionogels

The thermoelectric (TE) properties of the SWNT ionogels were characterized by applying a temperature gradient between the two ends of each sample. **Figures 2a**–**2e** and **Figure S10** summarize the corresponding open-circuit voltage (V_{oc}) profiles for SWNT ionogels of 0 to 2 wt%. For the ionogel without SWNT, V_{oc} rises gradually after the temperature gradient is applied and reaches a steady value of 10.1 mV at ΔT = 0.5 K after 629 s (**Figure 2a**). It then becomes constant after the temperature gradient becomes steady. The corresponding thermopower is 20.2 $mV \cdot K^{-1}$, which is consistent with the results reported in literature [41, 48]. Upon switching off the heater, the temperature gradient decays to zero, and V_{oc} correspondingly relaxes to zero over time. The observed V_{oc} response is attributed to ion accumulation at the two ends under a temperature gradient, namely the Soret effect.

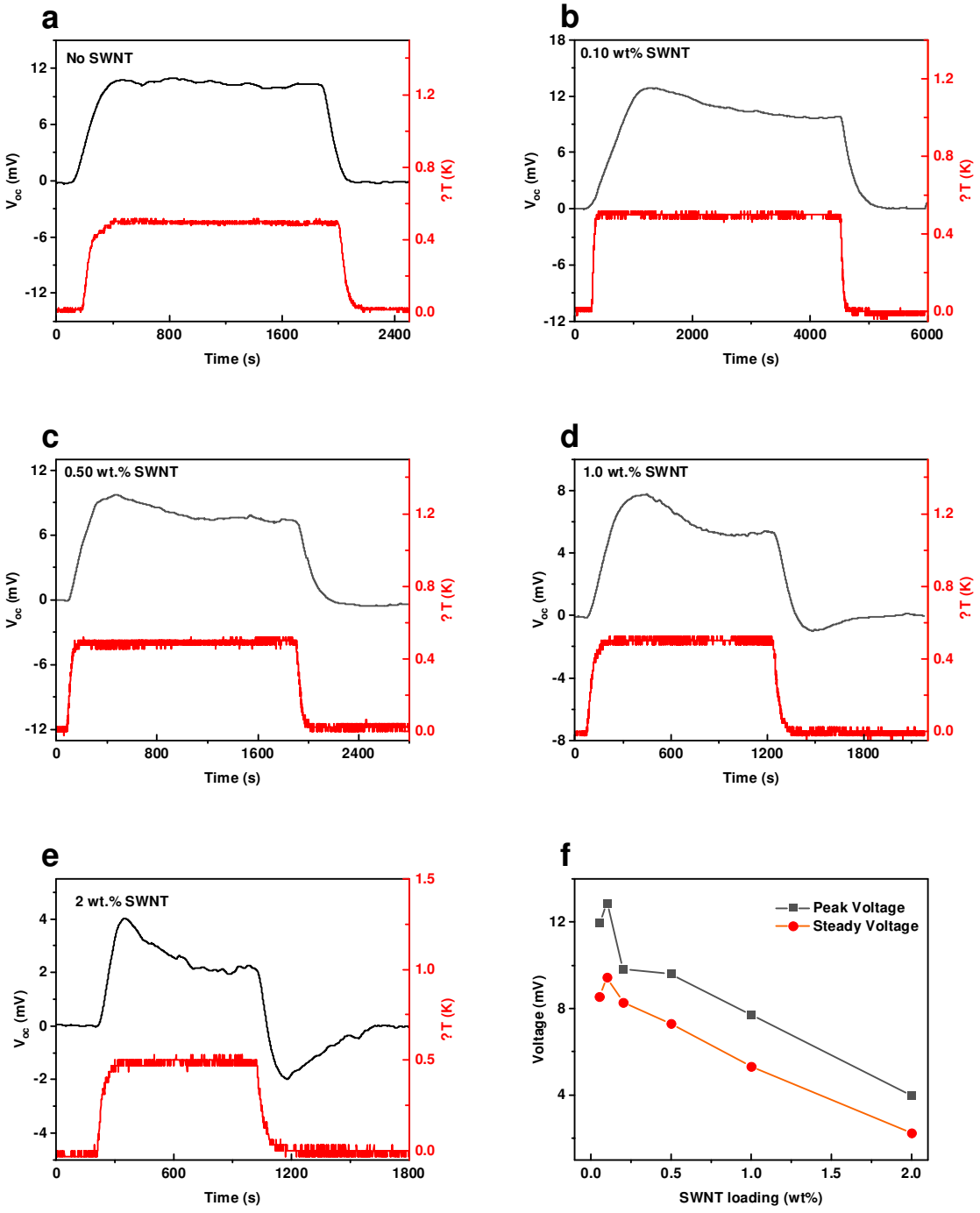


Figure 2. Temperature gradient and V_{oc} profiles of ionogels with SWNT loadings of (a) 0, (b) 0.10 wt%, (c) 0.50 wt%, (d) 1.0 wt%, and (e) 2.0 wt%, measured under ambient conditions at 70% relative humidity. (f) Peak and steady-state open-circuit voltages as a function of SWNT loading.

Introducing SWNTs into the ionogels substantially alters the V_{oc} response. At an SWNT loading of 0.10 wt%, a pronounced transient behavior is observed. Following application of the temperature gradient, V_{oc} rises to a peak of 12.9 mV (**Figure 2b**), then decreases and eventually stabilizes at 9.8 mV. The transient V_{oc} behavior becomes

more obvious for the ionogels with a higher SWNT loading [49]. At 0.5 wt% SWNTs, near the percolation threshold, V_{oc} attains a peak of 9.59 mV and subsequently relaxes to a steady value of 7.29 mV. For SWNT loadings of 0.8 wt% and above, V_{oc} becomes negative immediately after the heater is switched off (**Figures 2d**, **2e**, and **S10d-S10f**) and then gradually returns to zero.

The steady open-circuit voltage (V_{ocs}) was obtained by fitting the V_{oc} decay elaxation using an exponential function, $V_{oc} = V_0\, e^{-(t-t_0)/\tau} + V_{ocs}$, where V_0+V_{ocs} is the initial voltage at $t = t_0$, and τ is the time constant [41, 50]. Both the peak (V_{ocp}) and steady-state open-circuit voltages are dependent on SWNT loading. As shown in **Figure 2f**, both the peak and steady-state open-circuit voltages exhibit an overall decrease with increasing SWNT loading. The relaxation time constant as a function of SWNT loading is summarized in **Figure S11**. It increases from 625 s to 985 s when the loading rises from 0.05 wt% to 0.10 wt% and then decreases upon further increasing the SWNT content.

Previous studies have shown that water uptake can influence the thermoelectric behavior of ionic conductors [40, 51-54]. **Figure S12** presents the open-circuit voltage profiles of ionogels with 0.1 wt% SWNTs measured at $\Delta T = 3$ K under relative humidities (RH) of 40%, 55%, and 70%. Lowering the relative humidity leads to reductions in both the peak and steady-state open-circuit voltages. At 70% relative humidity, the peak and steady-state values are 59.3 mV and 39.7 mV, respectively, and they decrease to 35.4 mV and 24.9 mV at 40% RH. This trend is attributed to absorbed water facilitating ion dissociation and enhancing ionic migration.

It is important to distinguish the present results from those reported by Cheng et al [49]. In their study, single-walled carbon nanotube (SWNT) ionogels were investigated at SWNT loadings of 2 to 13 wt%, which are well above the percolation threshold of the SWNT network. By contrast, the present work concentrates on ionogels with SWNT loadings below 2 wt%. Consistent with Cheng et al., the open-circuit voltage of an ionogel containing 13 wt% SWNTs is essentially steady and can be attributed primarily to the Seebeck effect of the SWNT network [49]. Notably, the Seebeck coefficient of SWNT films is far smaller than the peak and steady-state open-circuit voltages obtained here in the low-loading regime. These comparisons indicate that the thermoelectric response in the sub-percolation regime differs fundamentally from that in the high-loading, fully percolated regime.

2.3 Transient and steady voltage behaviors

As discussed above, the transient open-circuit voltage response of the SWNT ionogels depends strongly on SWNT loading. Under an imposed temperature gradient, ions accumulate at opposite ends of the sample via the Soret effect. This ionic redistribution generates a potential difference from the cold end to the hot end, consistent with the *p*-type character of the SWNT ionogels. As a result, a SWNT locating a colder site has a potential higher than

the one with a higher temperature. When the SWNTs are separated far away, charges cannot transport across the SWNTs. Thus, they do not noticeably affect the V_{oc} profile. When the SWNTs are close and even form conductive paths, the thermovoltage (V_{th}) due to the Soret effect of the ions under temperature gradient can drive the holes across SWNTs from a cold to hot site. Under the open-circuit condition, the holes trap at the hot end and thus generate an internal voltage (V_{in}) opposite to the ionic thermovoltage. The open-circuit voltage is the sum of V_{th} and V_{in}, $V_{oc} = V_{th} + V_{in}$. The hole tunnelling depends not only the resistance but also the capacitance between the SWNTs and EMIM:DCA. Hence, V_{in} gradually increases over time, which causes the decay of V_{oc}. Based on this model, an equivalent circuit is proposed in **Figure 3a**.

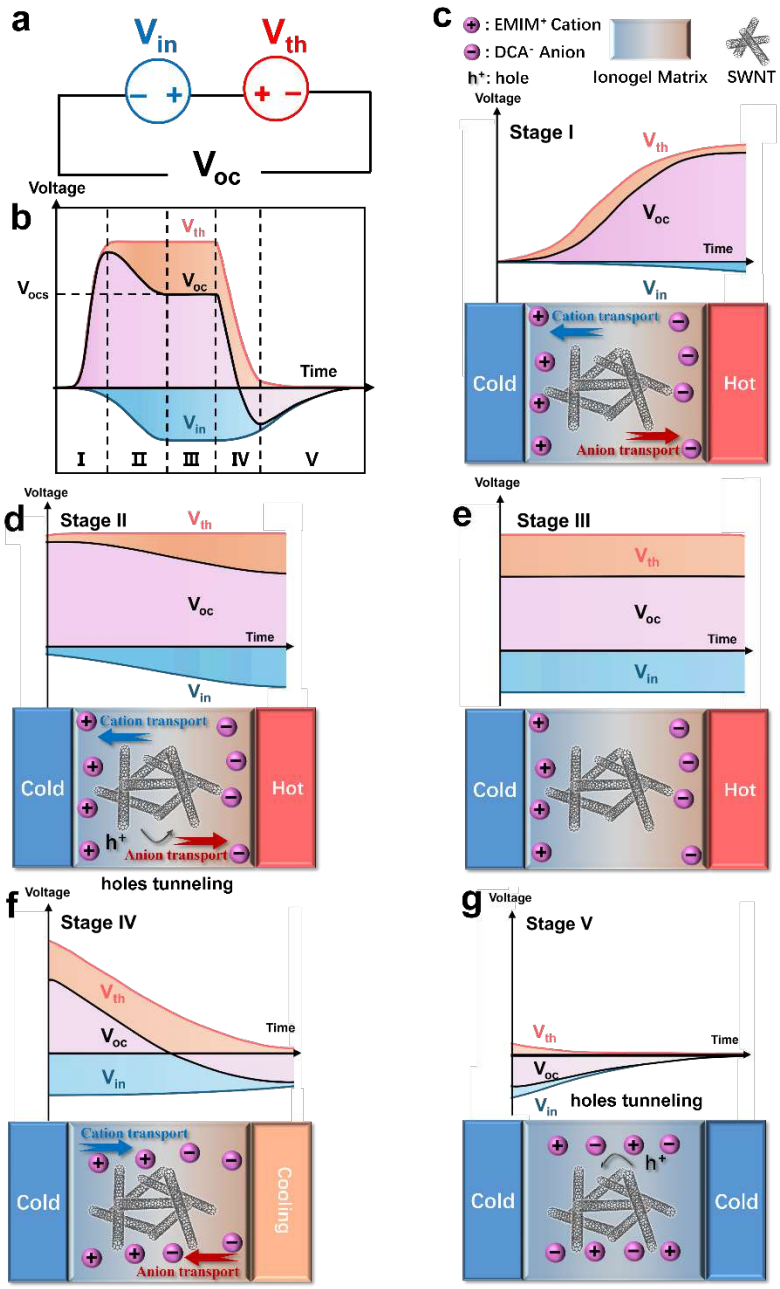


Figure 3. (a) Equivalent circuit describing V_{oc} generation in an SWNT ionogel under a temperature gradient. (b) Schematic evolution of V_{oc}, V_{th}, and V_{in} over the five stages of a thermal cycle. (c-g) Schematic illustrations of the formation of V_{th} and V_{in} in Stages I-V. The "+" and "–" without a circle signify a hole and electron, respectively, and h^+ represents a hole.

At low SWNT loadings, the open-circuit voltage can display a pronounced transient response. As illustrated in **Figure 3b**, the open-circuit voltage evolution can be separated into five stages. In Stage I, switching on the heater establishes a temperature gradient across the sample, leading to a rapid increase in open-circuit voltage. The initial increase is mainly attributed to thermodiffusion-induced ion accumulation at opposite ends of the ionogel (Soret effect). Meanwhile, the Seebeck effect drives hole redistribution within the SWNT network toward the cold end. Despite this electronic contribution, the open-circuit voltage is dominated by the ionic component because the ionic thermopower is roughly three orders of magnitude larger than the Seebeck coefficient of SWNTs. The thermovoltage generated by ionic accumulation drives hole transport along the SWNT pathways from the cold end toward the hot end. Under open-circuit conditions, these holes accumulate at the hot end, generating an internal voltage (V_{in}) that opposes the thermovoltage (V_{th}). During Stage I, V_{in} increases, but its growth is substantially slower than the initial rise of V_{th} (**Figure 3c**).

In Stage II, the temperature gradient stabilizes and the thermovoltage Vth reaches a steady value. Under this constant driving force, additional holes are transported from the cold end to the hot end. The charge-transfer dynamics are governed by the interfacial capacitance (C) at the SWNT-ionic liquid interface and the electronic resistance (R_e), associated with transport through the SWNT network. Consequently, the V_{oc} decreases progressively with time (**Figure 3d**).The time constant (τ) for the V_{oc} decay is related to R_e and C, $\tau = R_eC$. The capacitance of the SWNT ionogels increases approximately linearly with the SWNT volume fraction (ϕ), because the interfacial contact area between SWNTs and EMIM:DCA scales with SWNT loading (**Figure S13**).

In Stage III, hole accumulation at the hot end driven by the ionic thermovoltage reaches equilibrium. Consequently, the internal voltage V_{in} stabilizes, and the open-circuit voltage V_{oc} attains a steady value (**Figure 3e**). In Stage IV, the heater is turned off, leading to a decay of the temperature gradient. The ions then relax toward their initial distribution, resulting in a reduction of the ionic thermovoltage V_{th}. Because of the decrease of V_{th}, the holes trapped at the hot end migrate back through the SWNTs, and V_{in} thus decreases as well. However, V_{th} decreases much faster than V_{in} because the hole retreatment depends on the time constant. As a result, V_{oc} can drop to negative value (**Figure 3f**). The negative V_{oc} is a good evidence for the hole trapping at the hot end. At the stage

V, the retreatment of the trapped holes continues. The absolute V_{oc} value gradually decreases over time and finally becomes zero (**Figure 3g**).

To further validate the model, open-circuit voltage profiles were measured under a series of temperature gradients. **Figure S14** shows that the ionogel with 0.10 wt% SWNTs exhibits essentially no transient V_{oc} response at ΔT = 0.4 K, while a pronounced transient behavior appears when ΔT is increased to 0.85 K or higher. Moreover, the ratio of the steady-state open-circuit voltage (V_{ocs}) to the peak open-circuit voltage (V_{ocp}) decreases exponentially with increasing ΔT (**Figure S15**). This behavior supports the charge-tunneling picture, as higher temperature gradients enlarge the potential difference between adjacent SWNTs and thereby accelerate hole tunneling.

2.4 Thermoelectric performance of MTEGs

An MTEG was constructed by painting two silver electrodes onto the SWNT ionogel (**Figure 4a**). The thermoelectric responses of MTEGs based on ionogels with varying SWNT loadings are compiled in **Figures 4b** and **S16**. Measurements were performed under a rectangular thermal cycle with ΔT = 3 K and a cycle duration of 1500 s. The device response is highly sensitive to SWNT loading, and incorporation of SWNTs markedly alters the output-voltage (V_{op}) profile measured across an external load. For ionogels containing 0.02 wt% to 1.0 wt% SWNTs, the traces exhibit both transient and steady-state features, analogous to the open-circuit voltage behavior (**Figure S16**). **Figure 4b** shows the obtained on a 25 kΩ load for an MTEG with 0.10 wt% SWNTs. Consistent with the open-circuit case, the V_{op} evolution can also be partitioned into five stages. In Stage I, application of the temperature gradient causes to increase gradually to a peak. In Stage II, the temperature gradient is held constant and V_{op} decreases gradually with time. At the stage III, V_{op} reaches a steady value under the steady temperature gradient. In Stage IV, switching off the heater causes the temperature gradient to collapse to zero, and V_{th} drops rapidly and becomes negative. At the stage V, V_{op} relaxes from the negative minimum back to zero. This V_{op} evolution differs fundamentally from that of ionic thermoelectric capacitors (ITECs), for which the output voltage under a steady temperature gradient decays rapidly to zero and the response is typically described by a four-stage

profile.

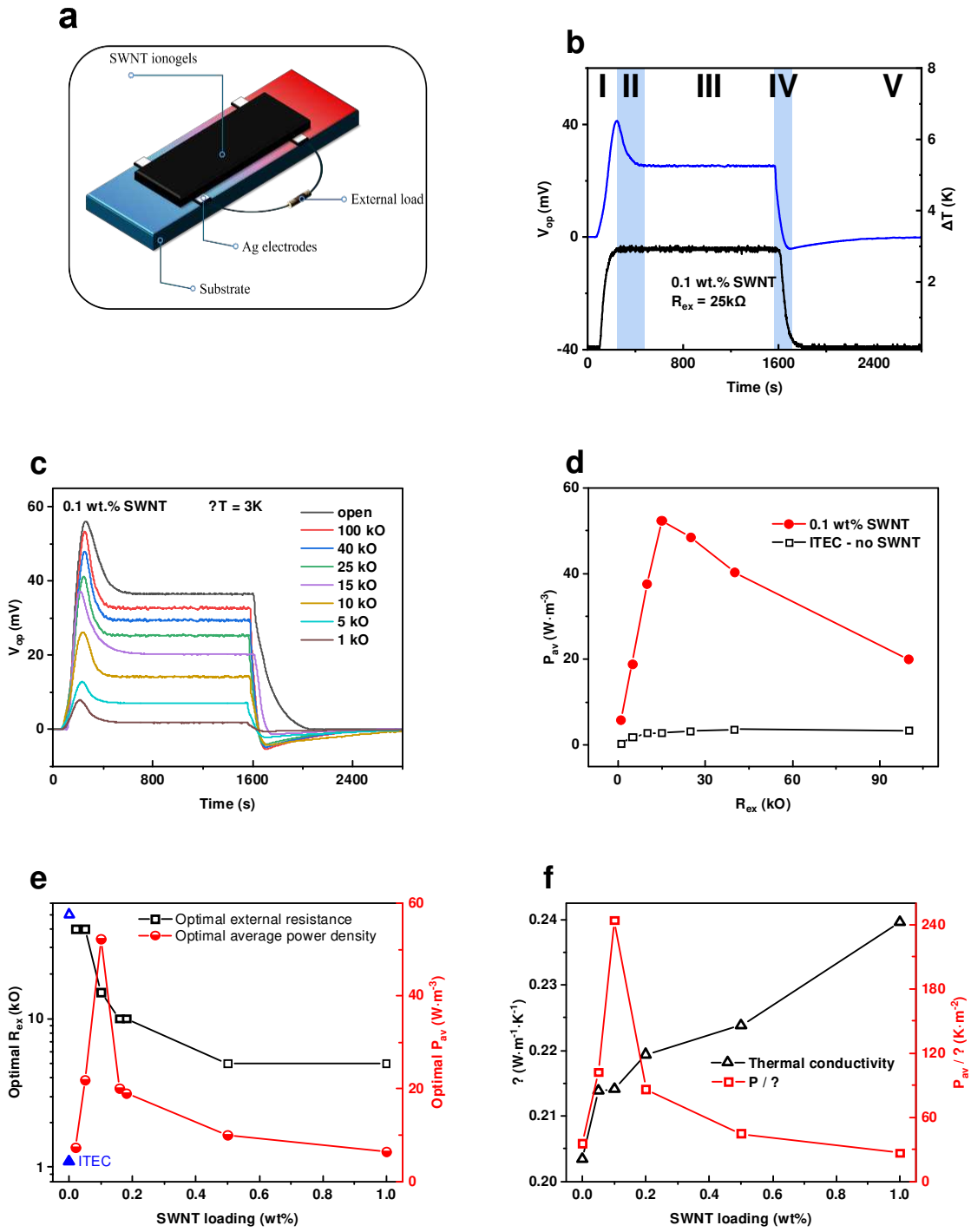


Figure 4. Thermoelectric performance of MTEGs. (a) An MTEG connected with an external load. V_{op} profiles measured under a rectangular thermal cycle for an MTEG with 0.1 wt% SWNTs using (b) a 25 kΩ load and (c) a series of external load resistances. (d) Average power density (P_{av}) as a function of external load resistance (R_{ex}) for the MTEG with 0.1 wt% SWNTs. (e) Optimal R_{ex} and corresponding optimal P_{av} as a function of SWNT loading, with the control ITEC without SWNTs shown for comparison. (f) Thermal conductivity (λ) of SWNT ionogels and P_{av} /λ of MTEGs as a function of SWNT loading.

As shown in **Figure 4c**, the peak (V_{opp}) and steady (V_{ops}) output voltages depend on the resistance (R_{ex}) of the external load. Both of them increase with the increasing R_{ex}. The average power densities (P_{av}) on the external load were calculated for a whole thermal cycle in terms of the equation [50],

$$P_{\mathrm{av}} = \frac{1}{VOL \cdot \Delta t} \int \frac{{V_{op}}^2 dt}{R_{\mathrm{ex}}}$$

where R_{ex} is the resistance of the external load, VOL the volume of the SWNT ionogel between electrodes, and Δt is the duration of the non-zero temperature gradient [41]. **Figures 4d** and **S17** show the variations of P_{av} with R_{ex} for the ionogels with different SWNT loadings. At each SWNT loading, the Pav increases with Rex to a maximum and then decreases. The highest P_{av} of 52.2 $W \cdot m^{-3}$ is obtained for the MTEG with 0.10 wt% SWNTs. This value is substantially higher than that of the ITEC based on the control ionogel without SWNTs, which yields 3.7 $W \cdot m^{-3}$. The enhancement is attributed to the steady output-voltage response of the MTEG under a steady temperature gradient. The maximum P_{av} of 52.2 $W \cdot m^{-3}$ also exceeds the reported value of 18.6 $W \cdot m^{-3}$ for reduced graphene oxide based MTEGs with a loading of 3.4 wt% [55].

The optimal P_{av} and the corresponding R_{ex} are plotted versus the SWNT loading for the MTEGs (**Figure 4e**) [56]. The optimal R_{ex} decreases monotonically with increasing SWNT loading. Specifically, the optimal external resistance is approximately 40 kΩ for the ionogel without SWNTs and decreases to 5 kΩ for SWNT ionogels containing 1.0 wt% SWNTs. In contrast, P_{av} shows a non-monotonic dependence on SWNT loading, increasing initially and then decreasing at higher loadings, with a maximum of 52.2 $W \cdot m^{-3}$ at 0.10 wt% SWNTs.

The thermal conductivity of the SWNT ionogels increases modestly with increasing SWNT loading (**Figure 4f**), which is attributed to the substantially higher thermal conductivity of SWNTs relative to EMIM:DCA and gelatin. The thermal conductivity is 0.20 $W \cdot m^{-1} \cdot K^{-1}$ for the ionogel without SWNTs and increases to 0.24 $W \cdot m^{-1} \cdot K^{-1}$ at an SWNT loading of 1.0 wt%. Since the thermal conductivity varies with SWNT content, comparing device performance using P_{av}/λ is more appropriate. Because λ changes only slightly over the examined loading range, the dependence of P_{av}/λ on SWNT loading closely follows that of P_{av} (**Figure 4f**). The MTEG with 0.10 wt% SWNTs achieves the highest P_{av}/λ of 244 $K \cdot m^{-2,}$ which is markedly higher than the reported value of 64.6 $K \cdot m^{-2}$ for reduced graphene oxide based MTEGs [55].

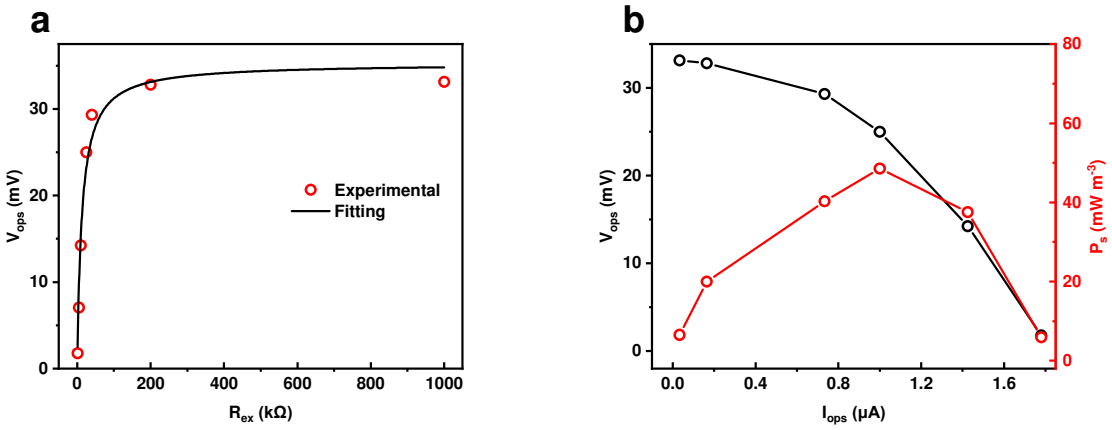


Figure 5. (a)V_{ops} as a function of R_{ex} for MTEGs based on ionogels containing 0.10 wt% SWNTs. (b) V_{ops} and P_s as a function of I_{ops} for MTEGs with 0.10 wt% SWNTs.

The V_{ops} values were extracted by fitting the output-voltage traces with an exponential decay, $V_{op} = V_1 e^{-(t-t_0)/\tau_1} + V_{ops}$, where V_1+V_{ops} is the initial output voltage and τ_1 is the time constant [41]. **Figures 5a** and **S18a** show V_{ops} as a function of R_{ex} for MTEGs based on ionogels containing 0.05 wt%, 0.10 wt%, and 0.50 wt% SWNTs. In all cases, V_{ops} increases with increasing R_{ex}. The V_{ops}-R_{ex} dependence is well described by a voltage-divider relation, $V_{ops} = V_{ocs}R_{ex}/(R_{ex}+R_{in})$, with R_{in} denotes the internal resistance. Fitting yields R_{in} values of 8.6 kΩ, 13.6 kΩ, and 11.3 kΩ for MTEGs with SWNT loadings of 0.05 wt%, 0.10 wt%, and 0.50 wt%, respectively. These values closely match the ionic resistances of the corresponding SWNT ionogels obtained from AC impedance spectroscopy, namely 7.8 kΩ, 12.9 kΩ, and 12.1 kΩ.

Figures 5b and **S18b** show the dependence of V_{ops} on the corresponding output current (I_{ops}). The resulting near-linear dependence is characteristic of conventional thermoelectric generators. The steady-state power density (P_s) is calculated from V_{ops} and I_{ops} using $P_s = V_{ops} I_{ops}$. The arch-like relationship between P_s and I_{ops} is like that of conventional TEGs as well. The optimal P_{av} values are 20.6, 48.6, and 17.1 mW m^{-3} for the MTEGs with the SWNT loadings of 0.05 wt%, 0.10 wt%, and 0.50 wt%, respectively, with the 0.10 wt% device delivering the highest steady-state power. This optimal P_s exceeds the value of 18.6 mW·m^{-3} reported for reduced graphene oxide based MTEGs by Qian et al.[55] and is comparable to the 50 mW·m^{-3} reported for silver nanowire based MTEGs [50].

The MTEGs operated under a steady temperature gradient can sustain a stable output voltage on an external load for extended durations. As shown in **Figure S19a**, an MTEG based on an ionogel containing 0.10 wt% SWNTs maintains an output voltage of 8.0 mV on a 25 kΩ load after 16 h of operation. In contrast, the control

ITEC exhibits a rapid voltage decay to zero within 1 h. The slow decline of V_{op} in the MTEG is attributed to the gradual relaxation of the SWNT ionogel open-circuit voltage with time (**Figure S19b**).

In terms of the experimental results, an equivalent circuit is formulated for the MTEGs (**Figure S20**), which is distinct from the standard circuit descriptions for ITECs and conventional TEGs (**Figure S21**). In this model, the SWNT ionogel sustains a steady output voltage under a steady temperature gradient, enabled by hole tunneling through the SWNT network. The device internal resistance is primarily determined by the ionic resistance of the SWNT ionogel and is in series with the external load. Accordingly, the V_{ocs} of an MTEG is comparable to the Seebeck voltage of a single-leg conventional TEG. For the MTEG with 0.10 wt% SWNTs, V_{ocs} reaches 35.2 mV at ΔT = 3 K, corresponding to a thermopower of 11.7 mV·K^{-1}, which is one to two orders of magnitude higher than the Seebeck coefficients of typical electronic thermoelectric materials. Although ionogels without electronic fillers can exhibit higher thermopower, they cannot provide continuous electrical output to an external load under steady temperature gradients. The steady output voltage shows a strong dependence on SWNT loading, with an optimum at 0.10 wt%. Notably, at this loading the ionogel supports electronic transport, yet its electronic conductivity remains low.

The MTEGs are very different from the combinatorial devices of an ITEC with a TEG as well. V_{op} of an ITEC decays to zero under steady temperature gradient[11]. Only the TEG can generate the Seebeck voltage, which is notably lower than 1 mV·K^{-1}[49]. MTEGs are also very different from thermogalvanic cells (TGCs). A TGC can generate electricity under steady temperature gradient, but the output voltage decays to zero in a few hours, and regeneration is needed [21, 57].

In addition to their distinct performance, MTEGs operate by a mechanism that differs from that of ITECs. **Figure S22** summarizes the ITEC response within a thermal cycle as four stages [58]. In this scheme, heat-to-electricity conversion is confined to Stages II and IV, and the output voltage is absent under a steady temperature gradient. In contrast, MTEGs produce electrical output under both fluctuating and steady gradients and sustain a stable voltage across an external load under steady conditions. This capability arises from the cooperative roles of EMIM:DCA and the SWNT conductive network.

3. Conclusion

EMIM:DCA/gelatin ionogels incorporating SWNTs operate as mixed ion and electron conductors. The ionic conductivity, electronic conductivity, and open-circuit thermovoltage vary with SWNT loading. When the SWNT content exceeds the electronic percolation threshold, the open-circuit thermovoltage exhibits a distinct transient component. MTEGs built from SWNT ionogels support continuous heat-to-electricity conversion under both

fluctuating and steady temperature gradients. Under steady gradients, they maintain a stable output voltage across an external load, analogous to conventional electronic TEGs. At 0.10 wt% SWNTs, the thermopower reaches 11.7 $mV \cdot K^{-1}$. This behavior is attributed to the combined contributions of hole tunneling through the SWNT network and the ionic Soret effect.

4. Materials and methods

Materials: Single-walled carbon nanotubes (SWNTs, Product Code: TNS) were purchased from Timesnano [56]. 1-ethyl-3-methylimidazolium dicyanamide (EMIM:DCA), gelatin, and sodium dodecyl sulfate (SDS) were supplied by Sigma-Aldrich [41]. Silver paste (PELCO 16062) was purchased from Ted Pella. All reagents were used as received.

Preparation of SWNT dispersion: SWNTs (30 mg) were dispersed in deionized water (6 mL) containing SDS (150 mg). The suspension was probe-sonicated at 140 W with 40% amplitude for 15 min to obtain a uniform SWNT/SDS dispersion.

Fabrication of SWNT ionogels: EMIM:DCA was mixed with an aqueous gelatin solution (2 wt%) at a gelatin to EMIM:DCA mass ratio of 2:8. The SWNT/SDS dispersion was then added and homogenized. The resulting mixture was drop-cast onto glass substrates sequentially cleaned with deionized water, isopropanol (IPA), and UV-ozone. Films were dried at room temperature for 12 h, followed by thermal treatment at 60 °C for 30 min and 120 °C for 30 min [56]. The obtained ionogel films had a thickness of approximately 45 μm.

Thermovoltage measurements: Thermovoltage was measured using a custom-built setup. Silver electrodes were painted on glass with a 1 mm gap and cured at 60 °C for 5 min. Voltage was recorded using a Keithley 2000 source/meter [56]. Temperatures at both ends were monitored using type-T thermocouples together with a UT325 thermometer.

The electronic conductivity of the SWNT/SDS films was measured by the van der Pauw four-probe method. AC impedance spectra were recorded on a Metrohm Autolab PGSTAT302N potentiostat/galvanostat with a 10 mV AC amplitude over 100 kHz-0.1 Hz. A SWNT ionogel film was sandwiched between two stainless-steel plates. The ionic resistance of the control ionogels without SWNTs was obtained in terms of the intercept on the axis of the real part of the ac impedance. The Nyquist plots [59] of the SWNT ionogels were analyzed with the equivalent circuit shown in **Figure 2e**. The ionic and electronic conductivities were then calculated using the equation,

$$\sigma = \frac{l}{\mathrm{R}A}$$

where σ is the ionic or electronic conductivity, l is the thickness, R is the corresponding resistance, and A is the electrode area.

Unless otherwise specified, thermovoltage and conductivity measurements were performed at room temperature under the relative humidity of 68–70%.

Microstructural and physical characterizations were carried out as follows: SEM (Zeiss SUPRA 40), ATR-FTIR (PerkinElmer FTIR spectrometer), and Raman spectroscopy (LabRAM HR Evolution, 514.5 nm excitation). The thermal conductivities of the ionogels were determined using a Hot Disk Thermal Constants Analyzer (TPS 2500S) employing the transient plane source (TPS) method. The sensor was positioned between two identical ionogel samples, and thermal conductivities were calculated based on the transient temperature data.

Fabrication of MTEGs and power calculation: The MTEGs were fabricated through a similar procedure for the samples during the measurement of thermovoltage. The average power densities for the MTEGs were calculated by using the equation [60]:

$$P_{\mathrm{av}} = \frac{1}{VOL\Delta t}\int \frac{{V_{op}}^2 dt}{R_{\mathrm{ex}}}$$

where R_{ex} is the resistance of the external load, VOL is the volume of the SWNT ionogel between electrodes, and Δt is the total duration of the thermal cycle. The thermal cycle had a rectangle profile with the temperature gradient of 3 K.

References

1. Forman C, Muritala IK, Pardemann R, Meyer B (2016) Estimating the global waste heat potential. Renew Sustain Energy Rev 57:1568-1579. https://doi.org/10.1016/j.rser.2015.12.192
2. Mulla R, Dunnill CW (2019) Powering the hydrogen economy from waste heat: A review of heat-to-hydrogen concepts. ChemSusChem 12:3882-3895. https://doi.org/10.1002/cssc.201901426
3. Biswas K, He J, Blum ID, Wu CI, Hogan TP, Seidman DN et al. (2012) High-performance bulk thermoelectrics with all-scale hierarchical architectures. Nature 489:414-418. https://doi.org/10.1038/nature11439
4. Han CG, Zhu YB, Yang L, Chen J, Liu S, Wang H et al. (2024) Remarkable high-temperature ionic thermoelectric performance induced by graphene in gel thermocells. Energy Environ Sci 17:1559-1569. https://doi.org/10.1039/D3EE03818A
5. Zhu Y, Han CG, Chen J, Yang L, Ma Y, Guan H et al. (2024) Ultra-high performance of ionic thermoelectric-electrochemical gel cells for harvesting low grade heat. Energy Environ Sci 17:4104-4114. https://doi.org/10.1039/D4EE01150C
6. Yu M, Li H, Li Y, Wang S, Li Q, Wang Y et al. (2024) Ionic thermoelectric gels and devices: Progress, opportunities, and challenges. EnergyChem 6:100123. https://doi.org/10.1016/j.enchem.2024.100123
7. Barlow J, Cameron GA (2003) Field experiments show that acoustic pingers reduce marine mammal bycatch in the California drift gill net fishery. Mar Mamm Sci 19:265-283. https://doi.org/10.1111/j.1748-7692.2003.tb01108.x
8. Malik YT, Akbar ZA, Seo JY, Cho S, Jang SY, Jeon JW (2022) Self-healable organic-inorganic hybrid thermoelectric materials with excellent ionic thermoelectric properties. Adv Energy Mater 12:2103070. https://doi.org/10.1002/aenm.202103070
9. Park TH, Kim B, Yu S, Park Y, Oh JW, Kim T et al. (2023) Ionoelastomer electrolytes for stretchable ionic thermoelectric supercapacitors. Nano Energy 114:108643. https://doi.org/10.1016/j.nanoen.2023.108643

10. Jeong M, Noh J, Islam MZ, Kim K, Sohn A, Kim W et al. (2021) Embedding aligned graphene oxides in polyelectrolytes to facilitate thermo-diffusion of protons for high ionic thermoelectric figure-of-merit. Adv Funct Mater 31:2011016. https://doi.org/10.1002/adfm.202011016
11. Akbar ZA, Jeon JW, Jang SY (2020) Intrinsically self-healable, stretchable thermoelectric materials with a large ionic Seebeck effect. Energy Environ Sci 13:2915-2923. https://doi.org/10.1039/C9EE03861B
12. Yang D, Su X, Li J, Bai H, Wang S, Li Z et al. (2020) Blocking ion migration stabilizes the high thermoelectric performance in Cu2Se composites. Adv Mater 32:2003730. https://doi.org/10.1002/adma.202003730
13. Hawkey A, Dash A, Rodríguez-Martínez X, Zhao Z, Champ A, Lindenthal S et al. (2024) Ion-exchange doping of semiconducting single-walled carbon nanotubes. Adv Mater 36:2404554. https://doi.org/10.1002/adma.202404554
14. Sang S, Bai C, Wang W, Khan SA, Wang Z, Yang X et al. (2024) Finger temperature-driven thermogalvanic gel-based smart pen: Utilized for identity recognition, stroke analysis, and grip posture assessment. Nano Energy 123:109366. https://doi.org/10.1016/j.nanoen.2024.109366
15. Ahn J, Cho S, Wu L, Li X, Lee D, Ha JH et al. (2024) Innovations in self-powered sensors utilizing light, thermal, and mechanical renewable energy. Nano Energy 129:110045. https://doi.org/10.1016/j.nanoen.2024.110045
16. Khelifi W, Luscombe CK (2024) Recent developments in indacenodithiophene- and indacenodithienothiophene-based donor-acceptor conjugated polymers: From design to device performance in organic electronics. Prog Polym Sci 151:101804. https://doi.org/10.1016/j.progpolymsci.2024.101804
17. Kawabata R, Li K, Araki T, Akiyama M, Sugimachi K, Matsuoka N et al. (2024) Ultraflexible wireless imager integrated with organic circuits for broadband infrared thermal analysis. Adv Mater 36:2309864. https://doi.org/10.1002/adma.202309864
18. Kim SL, Hsu JH, Yu C (2018) Thermoelectric effects in solid-state polyelectrolytes. Org Electron 54:231-236. https://doi.org/10.1016/j.orgel.2017.12.021
19. Chang WB, Evans CM, Popere BC, Russ BM, Liu J, Newman J et al. (2016) Harvesting waste heat in unipolar ion-conducting polymers. ACS Macro Lett 5:94-98. https://doi.org/10.1021/acsmacrolett.5b00829
20. Fang Y, Cheng H, He H, Wang S, Li J, Yue S et al. (2020) Stretchable and transparent ionogels with high thermoelectric properties. Adv Funct Mater 30:2004699. https://doi.org/10.1002/adfm.202004699
21. Han CG, Qian X, Li Q, Deng B, Zhu Y, Han Z et al. (2020) Giant thermopower of ionic gelatin near room temperature. Science 368:1091-1098. https://doi.org/10.1126/science.aaz5045
22. Li T, Zhang X, Lacey SD, Mi R, Zhao X, Jiang F et al. (2019) Cellulose ionic conductors with high differential thermal voltage for low-grade heat harvesting. Nat Mater 18:608-613. https://doi.org/10.1038/s41563-019-0315-6
23. Zhao D, Wang H, Khan ZU, Chen J, Gabrielsson R, Jonsson MP et al. (2016) Ionic thermoelectric supercapacitors. Energy Environ Sci 9:1450-1457. https://doi.org/10.1039/C6EE00121A
24. Cheng H, He X, Fan Z, Ouyang J (2019) Flexible quasi-solid-state ionogels with remarkable Seebeck coefficient and high thermoelectric properties. Adv Energy Mater 9:1901085. https://doi.org/10.1002/aenm.201901085
25. Eastman ED (1928) Theory of the Soret effect. J Am Chem Soc 50:283-291. https://doi.org/10.1021/ja01389a007
26. Jiang Q, Sun H, Zhao D, Zhang F, Hu D, Jiao F et al. (2020) High thermoelectric performance in n-type perylene bisimide induced by the Soret effect. Adv Mater 32:2002752. https://doi.org/10.1002/adma.202002752
27. Shen H, Xu K, Duan Y, Wu P, Qian Z, Chen Y et al. (2023) All-printed flexible hygro-thermoelectric paper generator. Adv Sci 10:2206483. https://doi.org/10.1002/advs.202206483
28. Wang Y, Dai Y, Li L, Yu L, Zeng W (2023) Proton-coupled electron transfer aided thermoelectric energy conversion and storage. Angew Chem Int Ed 62:e202307947. https://doi.org/10.1002/anie.202307947
29. Würger A (2021) Thermoelectric ratchet effect for charge carriers with hopping dynamics. Phys Rev Lett 126:068001. https://doi.org/10.1103/PhysRevLett.126.068001
30. Yusupov K, Vomiero A (2020) Polymer-based low-temperature thermoelectric composites. Adv Funct Mater 30:2002015. https://doi.org/10.1002/adfm.202002015
31. Shuang Y, Mori S, Yamamoto T, Hatayama S, Saito Y, Fons PJ et al. (2024) Soret-effect-induced phase change in a chromium nitride semiconductor film. ACS Nano 18:21135-21143. https://doi.org/10.1021/acsnano.4c03574
32. Yang X, Tian Y, Wu B, Jia W, Hou C, Zhang Q et al. (2022) High-performance ionic thermoelectric supercapacitor for integrated energy conversion-storage. Energy Environ Mater 5:954-961. https://doi.org/10.1002/eem2.12220
33. Wang Y, Yang L, Shi XL, Shi X, Chen L, Dargusch MS et al. (2019) Flexible thermoelectric materials and generators: Challenges and innovations. Adv Mater 31:1807916. https://doi.org/10.1002/adma.201807916
34. Zhao D, Würger A, Crispin X (2021) Ionic thermoelectric materials and devices. J Energy Chem 61:88-103. https://doi.org/10.1016/j.jechem.2021.02.022
35. Le Q, Cheng H, Ouyang J (2023) An ionic thermoelectric capacitor with continuous power generation for heat harvesting. Chem Eng J 469:143828. https://doi.org/10.1016/j.cej.2023.143828

36. Zhao D, Fabiano S, Berggren M, Crispin X (2017) Ionic thermoelectric gating organic transistors. Nat Commun 8:14214. https://doi.org/10.1038/ncomms14214
37. Wang S, Li Y, Yu M, Li Q, Li H, Wang Y et al. (2024) High-performance cryo-temperature ionic thermoelectric liquid cell developed through a eutectic solvent strategy. Nat Commun 15:1172. https://doi.org/10.1038/s41467-024-45432-7
38. Yu B, Duan J, Cong H, Xie W, Liu R, Zhuang X et al. (2020) Thermosensitive crystallization-boosted liquid thermocells for low-grade heat harvesting. Science 370:342-346. https://doi.org/10.1126/science.abd6749
39. Wang Y, Zhang Y, Xin X, Yang J, Wang M, Wang R et al. (2023) In situ photocatalytically enhanced thermogalvanic cells for electricity and hydrogen production. Science 381:291-296. https://doi.org/10.1126/science.adg0164
40. Qian Q, Cheng H, Le Q, Ouyang J (2023) Great enhancement in the thermopower of ionic liquid by a metal-organic framework. Adv Funct Mater 33:2303311. https://doi.org/10.1002/adfm.202303311
41. Zhang K, Qian Q, Xu C, Chen Z, Liu S, Ouyang J (2025) A mixed ion-electron thermoelectric generator with an activated carbon ionogel for heat harvesting from fluctuated and steady temperature gradients. Nano Energy 146:111527. https://doi.org/10.1016/j.nanoen.2025.111527
42. Li P, Paul DR, Chung TS (2012) High-performance membranes based on ionic liquid polymers for CO2 separation from flue gas. Green Chem 14:1052-1063. https://doi.org/10.1039/C2GC16354C
43. Cao Y, Morrissey TG, Acome E, Allec SI, Wong BM, Keplinger C et al. (2017) A transparent, self-healing, highly stretchable ionic conductor. Adv Mater 29:1605099. https://doi.org/10.1002/adma.201605099
44. He X, Cheng H, Yue S, Ouyang J (2020) Quasi-solid-state nanoparticle/(ionic liquid) gels with significantly high ionic thermoelectric properties. J Mater Chem A 8:10813-10821. https://doi.org/10.1039/D0TA04100A
45. Wang Y, Shan JW, Weng GJ (2015) Percolation threshold and electrical conductivity of graphene-based nanocomposites with filler agglomeration and interfacial tunneling. J Appl Phys 118:065101. https://doi.org/10.1063/1.4928293
46. Kyrylyuk AV, van der Schoot P (2008) Continuum percolation of carbon nanotubes in polymeric and colloidal media. Proc Natl Acad Sci USA 105:8221-8226. https://doi.org/10.1073/pnas.0711449105
47. Li J, Ma PC, Chow WS, To CK, Tang BZ, Kim JK (2007) Correlations between percolation threshold, dispersion state, and aspect ratio of carbon nanotubes. Adv Funct Mater 17:3207-3215. https://doi.org/10.1002/adfm.200700065
48. Liu S, Zhang M, Kong J, Li H, He C (2025) Giant power output from ionic/electronic hybrid nanocomposite thermoelectric converter under constant temperature gradient. Adv Sci 12:e2406589. https://doi.org/10.1002/advs.202406589
49. Cheng H, Ouyang J (2020) Ultrahigh thermoelectric power generation from both ion diffusion by temperature fluctuation and hole accumulation by temperature gradient. Adv Energy Mater 10:2001633. https://doi.org/10.1002/aenm.202001633
50. Yang G, Qian Q, Xu C, Zhang K, Su F, Liu C et al. (2025) Mixed ion-electron conductors with ultrahigh thermopower for heat harvesting from both fluctuated and steady temperature gradients. Chem Eng J 523:168809. https://doi.org/10.1016/j.cej.2025.168809
51. Cho C, Kim B, Park S, Kim E (2022) Bisulfate transport in hydrogels for self-healable and transparent thermoelectric harvesting films. Energy Environ Sci 15:2049-2060. https://doi.org/10.1039/D2EE00341D
52. Kim DH, Akbar ZA, Malik YT, Jeon JW, Jang SY (2023) Self-healable polymer complex with a giant ionic thermoelectric effect. Nat Commun 14:3246. https://doi.org/10.1038/s41467-023-38830-w
53. Zhao D, Sultana A, Edberg J, Chaharsoughi MS, Elmahmoudy M, Ail U et al. (2022) The role of absorbed water in ionic liquid cellulosic electrolytes for ionic thermoelectrics. J Mater Chem C 10:2732-2741. https://doi.org/10.1039/D1TC04466D
54. Liu Z, Cheng H, Le Q, Chen R, Li J, Ouyang J (2022) Giant thermoelectric properties of ionogels with cationic doping. Adv Energy Mater 12:2200858. https://doi.org/10.1002/aenm.202200858
55. Qian Q, Cheng H, Xie H, Wu Y, Fang Y, Le Q et al. (2025) A mixed ion/electron thermoelectric generator with ultrahigh steady thermopower by exploring both hole tunneling and ion accumulations. Adv Energy Mater 15:2404522. https://doi.org/10.1002/aenm.202404522
56. Cheng H, Yue S, Le Q, Qian Q, Ouyang J (2021) A mixed ion-electron conducting carbon nanotube ionogel to efficiently harvest heat from both a temperature gradient and temperature fluctuation. J Mater Chem A 9:13588-13596. https://doi.org/10.1039/D1TA02869C
57. Zhang Y, Sohn A, Chakraborty A, Yu C (2021) Colossal thermo-hydro-electrochemical voltage generation for self-sustainable operation of electronics. Nat Commun 12:5269. https://doi.org/10.1038/s41467-021-25606-3
58. Wang H, Zhao D, Khan ZU, Puzinas S, Jonsson MP, Berggren M et al. (2017) Ionic thermoelectric figure of merit for charging of supercapacitors. Adv Electron Mater 3:1700013. https://doi.org/10.1002/aelm.201700013
59. Gao H, Guo B, Song J, Park K, Goodenough JB (2015) A composite gel-polymer/glass-fiber electrolyte for sodium-ion batteries. Adv Energy Mater 5:1402235. https://doi.org/10.1002/aenm.201402235
60. Liu H, Shi X, Xu F, Zhang L, Zhang W, Chen L et al. (2012) Copper ion liquid-like thermoelectrics. Nat Mater 11:422-425. https://doi.org/10.1038/nmat3273

Supplementary Files

This is a list of supplementary files associated with this preprint. Click to download.

- CNTMTEGTFMSIanonymous.docx